



Atomic Ni and Cu co-anchored 3D nanoporous graphene as an efficient oxygen reduction electrocatalyst for zinc-air batteries

Journal:	<i>Nanoscale</i>
Manuscript ID	NR-ART-03-2021-001612.R1
Article Type:	Paper
Date Submitted by the Author:	21-Apr-2021
Complete List of Authors:	<p>Cheng, Yongtai; Shanghai Jiao Tong University, Wu, Haofei; Shanghai Jiao Tong University Han, Jiu-hui; Tohoku University, Zhong, Siying; University of Electronic Science and Technology of China, Physics Huang, Senhe; Shanghai Jiao Tong University, 200240 Chu, Shu-Fen; Shanghai Jiao Tong University Song, Shuangxi; Shanghai Jiao Tong University Reddy, Kolan; Shanghai Jiao Tong University, State Key Laboratory of Metal Matrix, School of Materials Science and Engineering Wang, Xiaodong; Shanghai Jiao Tong University, Wu, Shao-Yi; School of Physical Electronics, University of Electronics Science and Technology of China, Chengdu 610054, P.R. China Chengdu, China, Zhuang, Xiaodong; Shanghai Jiao Tong University, Johnson, Isaac; Johns Hopkins University Liu, Pan; WPI-AIMR, ; Shanghai Jiao Tong University, Chen, Mingwei; Johns Hopkins University, Materials Science and Engineering; Tohoku University, WPI-AIMR</p>

Atomic Ni and Cu co-anchored 3D nanoporous graphene as an efficient oxygen reduction electrocatalyst for zinc-air batteries

Yongtai Cheng^{a, †}, *Haofei Wu*^{a, †}, *Jiuhui Han*^{b, c, †}, *Siyang Zhong*^d, *Senhe Huang*^e, *Shufen Chu*^a, *Shuangxi Song*^a, *Kolan Madhav Reddy*^a, *Xiaodong Wang*^a, *Shaoyi Wu*^d, *Xiaodong Zhuang*^e, *Isaac Johnson*^{c, f}, *Pan Liu*^{a, *}, *Mingwei Chen*^{f, *}

^a Shanghai Key Laboratory of Advanced High-temperature Materials and Precision Forming, State Key Laboratory of Metal Matrix Composites, School of Materials Science and Engineering, Shanghai Jiao Tong University, Shanghai 200240, P. R. China

^b Frontier Research Institute for Interdisciplinary Sciences (FRIS), Tohoku University, Sendai 980-8577, Japan

^c WPI Advanced Institute for Materials Research, Tohoku University, Sendai 980-8577, Japan

^d School of Physics, University of Electronic Science and Technology of China, Chengdu, Sichuan 611731, P. R. China

^e School of Chemistry and Chemical Engineering, Shanghai Jiao Tong University, Shanghai 200240, P. R. China

^f Department of Materials Science and Engineering, Johns Hopkins University, Baltimore, Maryland 21218, United States

* Corresponding authors

E-mail address: panliu@sjtu.edu.cn (P. Liu) , mwchen@jhu.edu (M.W. Chen).

† These authors contributed equally to this work.

ABSTRACT

Highly-active, cost-effective and durable electrocatalysts for the oxygen reduction reaction (ORR) is critically important for renewable energy conversion and storage. Here we report a 3D bicontinuous nitrogen doped nanoporous graphene electrocatalyst co-anchored with atomically dispersed nickel and copper atoms ((Ni,Cu)-NG) as a highly active single-atom ORR catalyst, fabricated by the combination of chemical vapor deposition and high temperature gas transportation. The resultant (Ni,Cu)-NG exhibits exceptional ORR activity in alkaline electrolytes, comparable to the Pt-based benchmarks, from the synergistic effect of the CuN_x and NiN_x complexes. Endowed by the high catalytic activity and outstanding durability in harsh electrochemical environments, the rechargeable Zinc-air batteries using (Ni,Cu)-NG as the cathodes show excellent energy efficiency (voltage gap of 0.74 V), large power density (150.6 mW cm^{-2} at 250 mA cm^{-2}) and high cycling stability (>500 discharge-charge cycles at 10 mA cm^{-2}). This study may pave an efficient avenue of designing highly durable single-atom ORR catalysts for metal-air batteries.

Keywords: 3D nanoporous graphene, single atom catalyst, synergetic effect, oxygen reduction reaction, Zn-air battery

1. Introduction

Developing high-efficiency energy conversion technology is critically important in solving the challenges of environment and energy.¹⁻⁹ As one of the key cathodic reaction of promising green energy conversion devices such as fuel cells and metal-oxygen batteries, the oxygen reduction reaction (ORR) is a bottleneck in these renewable and eco-friendly technologies due to the sluggish reaction kinetics and thus large overpotentials and poor energy efficiency.¹⁰⁻¹³ Although noble metal platinum and its alloys are recognized as the most efficient catalysts for ORR by far,¹⁴⁻¹⁷ the high cost, natural scarcity and insufficient long-term durability have severely impeded their large-scale practical applications. Thus, it is of great significance to develop high-efficiency and low-cost ORR alternative catalysts. Up to now, enormous attempts have been made in search for high-performance Pt-free ORR catalysts. Among them, nitrogen doped carbon materials supported non-precious transition metal single-atom catalysts (TM-NCs) have aroused great interest owing to high ORR catalytic activity and low material costs.¹⁸⁻²⁵ It has been suggested that the MN_xC_y moieties in TM-NCs play a pivotal role in activating O_2 and modulating binding energy of reaction intermediates in ORR.^{26,27} In combination with the intrinsically high electrical conductivity, lightweight, excellent electrochemical stability and large specific surface area of the carbon matrix,²⁸ TM-NCs are emerging as the promising candidates with both outstanding ORR catalytic activity and high durability to substitute Pt-based catalysts.²⁹ Various synthetic strategies have been developed to fabricate highly active TM-NCs in recent years. For example, Li et al. reported a facile host-guest strategy to fabricate a N-coordinated Fe-Co dual sites catalyst with superior ORR performance and ultra-long cycle stability (>50000 cycles) in acid environments.³⁰ Density functional theory (DFT) calculations revealed that the Fe-Co dual sites reduced the O-O cleavage barrier and favored the four-electron ORR path with a high selectivity. Similarly, Zn-Co metal atom pairs embedded in the sulfur-modified carbon, prepared by a simultaneous coordination pyrolysis approach, displayed exceptional ORR performance, surpassing the noble metal-based benchmark.³¹ In another case, Fe- N_x -C/Co- N_x -C³² or Fe- N_x -C/Ni- N_x -C³³ isolated dual atomic catalysts were reported to have the enhanced ORR activity from the synergistic effect of the heterogeneous metal-nitrogen coordinated active sites. It appears that the dual transition metal atoms supported by nitrogen doped carbon materials form effective atomic configurations with enhanced ORR performance, in addition to increasing the loading amount of active atoms, by breaking the limit of single atom catalysts (SACs).^{34,35} However, it still remains challenging to fabricate dual transition metal single catalysts on stable carbon supports, such as graphene, in a controllable manner.

Herein, we report a nitrogen doped nanoporous graphene with atomically dispersed Cu and Ni atoms ((Ni,Cu)-NG) prepared by chemical vapor deposition and subsequent high temperature gas transportation. The dual atomic electrocatalyst exhibits excellent ORR performance with the half-wave potential comparable to the commercial Pt/C catalysts in alkaline electrolytes. Benefiting from the high ORR electrocatalytic activity, together with outstanding conductivity, durability and mechanical stability, the (Ni,Cu)-NG catalyst as the cathodes of rechargeable zinc-air batteries offer excellent energy efficiency and long-cycle stability, surpassing the Pt/C counterparts. This work may provide inspirations for the rational design of high-performance single atom catalysts towards critical electrocatalytic reactions related to energy and environments.

2. Results and discussion

The nitrogen doped nanoporous graphene with anchored single Ni atoms was first fabricated by a nanoporous metal-based CVD method with controlled acid-wash treatment.³⁶⁻³⁸ Subsequently, the second heterogeneous Cu single atoms were loaded by a high-temperature gas transportation method, which has recently been proven to be an facile method to directly transform metal oxide (such as Cu₂O) to anchored single atoms on carbon-based supports.³⁹ Specifically, the CVD growth of N-doped nanoporous graphene was conducted at 800°C by utilizing dealloyed nanoporous Ni as the template and melamine as the carbon and nitrogen sources (**Fig. S1**). After dissolving the nanoporous Ni template in a 2 mol L⁻¹ HCl solution for 10 hours at ambient temperature, the nitrogen doped nanoporous graphene with residual single Ni atoms (Ni-NG) was obtained.³⁷ For comparison, the nitrogen doped nanoporous graphene (NG) with negligible residual Ni atoms was also prepared by dissolving Ni in a mixed solution of HCl and ferric chloride at 50 °C. The Ni-NG or NG were subsequently employed as the supports to fabricate (Ni,Cu)-NG or copper anchored NG (Cu-NG) using a Cu₂O based gas transportation method (**Fig. S2**), which has been detailed in the **Supplementary Information**. The concentrations of metal elements were determined to be 1.53 wt.% Cu and 0.60 wt.% Ni for (Ni,Cu)-NG, and 1.75 wt.% Cu and 0.10 wt.% Ni for Cu-NG, by inductively coupled plasma atomic emission spectroscopy (ICP) analyses (**Table S1**). In particular, the high loading amount of ~2.13 wt.% single-atom Ni and Cu are loaded into the N-doped nanoporous graphene.

The scanning electron microscope (SEM) images in **Fig. 1a** and **1b** show the microstructure of Ni-NG before and after dissolving the nickel template. The continuous nanotubular graphene inherits the nanoporous skeleton of nanoporous Ni with pore sizes ranging from 300 nm to 800 nm. The thickness of the Ni-NG sheet was measured to be about 80 μm (**Fig. 1c**). After the high

temperature gas transportation treatment and the introduction of single-atom copper, the nanoporous graphene substrates retain the nanoporous morphology without any visible structural collapse or damage (**Fig. 1d** and **Fig. S3**). No obvious nanoparticles were observed under transmission electron microscope (TEM) observations. The selected area electron diffraction (SAED) pattern presents sharp diffraction spots (**Fig. 1d**, inset), implying high crystallinity of Ni and Cu co-anchored nanoporous graphene. The high resolution TEM (HRTEM) image in **Fig. S4** reveals that the nanoporous graphene is mainly constructed by few-layer graphene. As a result of high curvatures, the nanoporous graphene possesses a high density of topological and geometric defects, as shown in **Fig. 1e**. These defects are the preferred sites for chemical dopants and, thus, are often enriched with nitrogen (and/or Ni) dopants. Upon the high temperature gas transportation treatment, the high chemical activities of the defects as well as nitrogen dopants are expected to promote the reduction of Cu oxide species to form relatively stable (Cu, Ni) N_xC_y or CuN_xC_y moieties with a high density of dispersions and a large loading amount.

The anchored Ni and Cu atoms were characterized by Cs-corrected high angle annular dark field scanning TEM (HAADF-STEM). As shown in **Fig. 1f**, the Ni or Cu atoms with relatively higher Z contrast atomically dispersed on the curved graphene substrate. Few of metal nanoclusters could be detected in our experiment, which may form when single atoms are close to each other. Several single atoms and their neighboring single atoms are highlighted by white rectangles. The average distance between the single atom and its neighboring single atom is calculated to be about 0.7nm from the intensity profile of the HAADF image (**Fig. S5 and S6**). Considering the slight difference between atomic number of nickel ($Z=28$) and copper ($Z=29$), it is rather challenging to identify Cu or Ni single atoms in the Z -contrast STEM image.⁴⁰ Energy dispersive spectrometer (EDS) elemental mappings were conducted to probe the distribution of each element. As depicted in **Fig. 1g**, C, N and Cu elements show uniform distributions in our sample. The Ni mapping shows a relatively low signal to noise ratio (SNR), due to the low doping concentration of nickel, and the EDS result with extended sampling time displays a better SNR (**Fig. S7**). Electron energy loss spectroscopy (EELS) results also verified that Cu, Ni and N elements co-exist in the nanoporous graphene (**Fig. S8**).

The X-ray diffraction (XRD) pattern (**Fig. S9**) of (Ni,Cu)-NG exhibits a single peak at about 26.2° , corresponding to graphitic carbon (002), and no other characteristic peaks related to Cu or Ni species were observed, indicating the absence of undesired metal nanoparticles. The Raman spectrum of the (Ni,Cu)-NG sample shows characteristic peaks of graphene at 1350

cm^{-1} (D band), 1576 cm^{-1} (G band) and 2689 cm^{-1} (2D band) without any discernible amorphous carbon features (**Fig. 2a**). The intensity ratio of 2D band to G band (I_{2D}/I_G) is determined to be 0.29, verifying that as-prepared sample is mainly few-layer graphene, consistent with the HRTEM results and previous works.^{41,42} As demonstrated in **Figure 2a**, after high temperature gas transportation to introduce copper, the (Ni,Cu)-NG and Cu-NG have lower D to G band intensity ratios (I_D/I_G) compared with pristine nanoporous graphene (NG), which could be attribute to the removal of residual oxygen function groups at high temperature.⁴³ X-ray photoelectron spectroscopy (XPS) was carried out to gain more insights into the chemical composition and electronic states of (Ni,Cu)-NG. As shown in **Fig. S10**, the C 1s high-resolution spectrum displays three main peaks, corresponding to sp^2 hybridized carbon, C-N and C=O.⁴⁴ A noticeable small bump could also be observed in the low binding energy region (283.4 eV), which may result from the C-Cu bonding.^{45,46} The high-resolution N 1s spectrum in **Fig. 2b** can be deconvoluted into four typical characteristic peaks of pyridinic N (398.5 eV), metal-N (399.1 eV), pyrrolic N (399.7 eV) and graphitic N (401.4 eV),^{47,48} with the fractions of 27.2%, 19.6%, 9.7% and 43.5%, respectively. The total amount of nitrogen in (Ni,Cu)-NG was measured to be 2.8 at.%. It is worth noting that pyridinic N, representing a considerable proportion in our sample, is commonly believed to be the coordinating sites for transition metals (M) to form M-N coordination structures with favorable catalytic activities.⁴⁹ As depicted in **Fig. 2c** and **Fig. 2d**, no metallic Ni or Cu signals were detected in (Ni,Cu)-NG. The Ni $2p_{3/2}$ peak at 853.7 eV, located between those of Ni^0 (852.6 eV) and Ni^{2+} (855.8 eV), indicates that the anchored Ni is ionic $\text{Ni}^{\delta+}$ ($0 < \delta < 2$), which may result from the N- or C-coordination.^{38,50} Similar to Ni, the location of Cu $2p_{3/2}$ peak agrees well with previously reported atomically dispersed Cu-N-C coordination motifs.^{51,52}

The extended X-ray absorption fine structure (EXAFS) measurements were utilized to unveil the local atomic structure of (Ni,Cu)-NG. The Fourier transform k^3 -weighted EXAFS for Cu exhibits a main peak at 1.56 \AA (**Fig. 2f**), which is obviously distinct from the Cu-Cu coordination in face-centered cubic metal Cu at 2.23 \AA and can be ascribed to Cu-N or Cu-C first shells.^{53,54} Similarly, no Ni-Ni coordination features were observed in the EXAFS spectrum of Ni (**Fig. 2e**), and the main peak at 1.38 \AA arises from the backscattering interaction between Ni and light atoms of N and/or C,^{55,56} rather than Ni-Ni and Ni-Cu. The EXAFS results, combined with XRD, XPS and HRTEM, evidence the atomically dispersed nature of both Cu and Ni species in the nitrogen doped nanoporous graphene. The detailed coordination configurations of (Ni,Cu)-NG was further explored by least-squares EXAFS fitting. Considering the Ni-N coordination observed in XPS and EXAFS, a Ni-N_x structure may

speculatively be formed. We found that a Ni-N₃ structural model (**Fig. 2e**, inset), i.e. one Ni atom coordinating with 3 N atoms, best fits the Ni K-edge EXAFS spectrum. Similarly, based on a Cu-N₂-V model (V: vacancy, **Fig. S14**) as suggested by previous research,⁴¹ we optimized the structure and demonstrated that a Cu-N₂-C₂ configuration offer the best consistency with all the experimental results (**Fig. 2f**, inset). The details about the computational models were further elaborated in the **Supplementary Information**. The least-squares fittings match well with the experimental EXAFS curves (**Fig. 2e** and **2f**), which validates that each Ni atom coordinates with three N atoms to form the Ni-N₃ structure with a bonding length of 1.87 Å while each Cu atom bonds to two N atoms and two C atoms to form a Cu-N₂-C₂ configuration.

The ORR electrocatalytic performances of (Ni,Cu)-NG were evaluated by cyclic voltammetry (CV) in O₂ and Ar-saturated 0.1 mol L⁻¹ KOH aqueous solutions (**Fig. S11**). Compared with the smooth curve under Ar saturation, a notable oxygen reduction peak at 0.78V can be observed in the O₂-saturated condition, revealing the electrocatalytic activity of (Ni,Cu)-NG towards ORR. Linear sweep voltammetry (LSV) measurements were subsequently implemented using the rotating disk electrode (RDE) technique. NG, Ni-NG, Cu-NG, nanoporous graphene without any dopants (G), and commercial Pt/C were tested under the same condition for comparison. The loading amount of each catalyst is 0.36 mg cm⁻². As illustrated in **Fig. 3a**, G and NG exhibit rather inferior ORR performances. In contrast, Cu-NG and (Ni,Cu)-NG demonstrate much higher electrocatalytic activities with conspicuous positive shifts of polarization curves, which further demonstrates that the introduction of the single-atom transition metal species boosts the ORR activity.^{51,57} Noticeably, the half-wave potential ($E_{1/2}$) of (Ni,Cu)-NG was measured to be 0.840 V (**Fig. 3e**), which surpasses that of commercial Pt/C ($E_{1/2} = 0.835$ V) under our experiment condition. When compared with other reported Pt-free catalysts, the (Ni,Cu)-NG also exhibits an excellent ORR activity (**Table S4, Supplementary Information**). RDE measurements at different rotation speeds were performed to investigate the ORR catalytic kinetics of (Ni,Cu)-NG (**Fig. 3b**). The highly linear and parallel Koutecky-Levich fitting plots (**Figure 3b**, inset) validate a first-order reaction kinetics towards the concentration of dissolved oxygen in the electrolyte.^{30,50} Additionally, at the potential of 0.8 V, the (Ni,Cu)-NG catalyst demonstrates a much larger kinetics current (5.65 mA cm²) than that of Pt/C (4.75 mA cm²) (**Fig. 3e**). The electron transfer number (n) were calculated to be 3.94-3.98 in the potential ranging from 0.2 V to 0.8 V by a rotating ring-disk electrode (RRDE) technique (**Fig. 3c**), corresponding to a H₂O₂ yield below 4% (**Fig. 3d**). It suggests the direct four electrons transfer pathway for the oxygen reduction. The electrocatalytic durability testing of (Ni,Cu)-NG shows that after 5000 CV scans between 0.2 V and 1.2 V, only slight current

decrease can be observed while the half-wave potential ($E_{1/2}$) remained almost the same (**Fig. 3f**), demonstrating the excellent robustness of (Ni,Cu)-NG.

To explore the nature of enhanced ORR catalytic activity of (Ni,Cu)-NG and identify the possible active sites, density function theory (DFT) calculations were carried out. The possible structures of catalytic CuN_x and NiN_x active sites in (Ni,Cu)-NG were first investigated, respectively. For the CuN_x active site, based on XPS and EXAFS results, the formation energy of various structure of $\text{CuN}_x\text{C}_{4-x}$ ($x=1,2,3$) were calculated. Among all the possible structures, the CuN_3C_1 and CuN_2C_2 (**I**) (**Fig. S15**) with the negative formation energy were the most energetically stable configurations. Considering a relative inferior theoretical performance for ORR of CuN_3C_1 among $\text{CuN}_x\text{C}_{4-x}$ structures,⁵⁸ the CuN_2C_2 (**I**) configuration is considered to be the possible active site in (Ni,Cu)-NG, which is also in line with the EXAFS fitting. For the NiN_x active site, the coordination number is determined to be 3.1 from the EXAFS fitting. Our previous work has demonstrated that Ni atoms in the Ni single atom anchored graphene fabricated by acid etching could occupy carbon sites in the honeycomb lattice of graphene.³⁶ Thus, the NiN_x active site is identified to be NiN_3 . To gain an insight into ORR mechanism of (Ni,Cu)-NG and the observed synergistic effect, the computational model consisting of heterogeneous Ni- N_3 and Cu- N_2 - C_2 structure embedded in the in-plane graphene matrix was constructed according to previous discussion. Single metal (Cu or Ni) anchored models were also built for comparison (**Fig. 4a**). The distance between two metal atoms in each model is initially set to be 0.672 nm based on HADDF results. More computational details are included in the **Supplementary Information**, and the optimized adsorption structure of the ORR intermediates for each catalytic site is presented from **Fig. S16** to **Fig. S19**. As show in the ORR Gibbs free energy diagram with the applied potential $U=0$ V (**Fig. 4b**), the Cu- N_2 - C_2 site in the both heterogeneous dual-metal doped model (Cu@NiCu-NG) and single atom doped model (Cu@Cu-NG) exhibits a similar continuous downhill trend, while an uphill endothermic step corresponding to the formation of OH^- is observed for Ni@Ni-NG and Ni@NiCu-NG. For Cu@NiCu-NG, the rate-limiting elementary step is determined to be the formation of *OOH with the highest Gibbs free energy change ($\Delta G=-0.19$ eV). In contrast, the energy barrier of rate-limiting OH^- formation sub-step for Ni@NiCu-NG is calculated to be 0.49 eV, higher than that of Cu@NiCu-NG, which suggests that the Cu- N_2 - C_2 site is more catalytic active for ORR and possibly works as the main active site. Accordingly, Cu@NiCu-NG possesses the highest onset potential among all catalytic sites (**Table. S2**). More importantly, From the ORR Gibbs free energy diagram (**Fig. 4b**) and the calculated onset potential, the synergistic effect is

observed for both Cu-N₂-C₂ and Ni-N₃ sites. For the Cu-N₂-C₂ site, the introduction of Ni-N₃ reduces the energy required to drive the rate-limiting step from -0.13 eV to -0.19 eV, and the situation is similar for Ni-N₃ sites. The origin of the synergistic effect may be attributed to the redistributed charge density around the central metal atom (**Fig. 4c, S20**).

Finally, to demonstrate the potential of (Ni,Cu)-NG for practical applications, a rechargeable Zn-air battery (ZABs) was assembled using the cloth paper loaded with (Ni,Cu)-NG catalyst ink (1.0 mg cm⁻²) as the cathode, a zinc plate as the anode and 6 mol L⁻¹ KOH solution with 0.1 mol L⁻¹ zinc chloride as the electrolyte (**Fig. 5a and S21**). The Zn-air battery exhibits an open-circuit voltage of 1.427 V (**Fig. S22**) and a maximum power density of 150.6 mWcm⁻² at the current density of 250 mA cm⁻², which exceeds the Pt/C counterpart (110.7 mWcm⁻² at 165 mA cm⁻²) (**Fig. 5b**). Meanwhile, as shown in the galvanostatic discharge curves in **Fig. 5c**, the (Ni,Cu)-NG based Zn-air battery delivers a specific capacity of 677 mAh g_{Zn}⁻¹ at 100 mA cm⁻², which outperforms the Pt/C based battery (581 mAh g_{Zn}⁻¹). The rechargeability and cycle durability of Zn-air batteries are also the key factors for commercial implementation. After more than 85 hour charging and discharging (more than 500 cycles) at 10 mA cm⁻², the charge and discharge voltages of (Ni,Cu)-NG based ZABs were measured to be ~1.94V and ~1.20V. Correspondingly, the voltage gap is as low as 0.74 V (**Fig. 5e and S23**) and the voltaic efficiency (the ratio of discharge voltage to charge voltage) is 61.9%, confirming the high electrocatalytic activities of (Ni,Cu)-NG and the superior cycle stability of the (Ni,Cu)-NG based ZABs. In contrast, the Pt/C+IrO₂ based ZABs delivered a relatively inferior performance with a larger voltage gap of 0.95 V and a lower voltaic efficiency of 54.7% after 40-hour charge-discharge cycling (**Fig. S24**).

3. Conclusions

In summary, an innovative and highly active (Ni,Cu)-NG electrocatalyst with atomically dispersed Cu and Ni species was successfully synthesized through CVD and subsequent high temperature gas transportation strategy. The co-existence of the isolated CuN_x and NiN_x species in the (Ni,Cu)-NG electrocatalyst, confirmed by HAADF-STEM, EELS, EDS and XAFS, generates a synergetic effect in ORR electrocatalysis. Compared with the inert NG, the Cu-N₂-C₂ and Ni-N₃ active sites in (Ni,Cu)-NG exhibit high ORR activity and outstanding stability in alkaline environments. Furthermore, the (Ni,Cu)-NG based rechargeable zinc-air batteries with a low catalyst loading amount displays an high specific capacity (677 mAh g_{Zn}⁻¹ at 100 mA cm⁻²) and long-cycle stability (>500 cycles), benefiting from the high ORR activity of (Ni,Cu)-NG. This work may pave an avenue towards rational design of high-performance single-atom

transition metal catalysts for ORR and emerging electrocatalytic reactions, such as oxygen evolution reactions and CO₂ reduction reactions.

Author contributions

Y.T. C, H.F. W and J.H. H contributed equally to this work. Y. C and H. W performed experiments, synthesized materials and wrote the draft. J. H performed formal analysis and helped with the revise of the original draft. S. Z, S. H and S. W. conducted the DFT calculation. F. C conducted the STEM characterization. S. S, K. R and X. W provided useful advice and expertise. X. Z contributed to the EXAFS analysis. M. C. and P. L supervised the experiment, directed the study and revised the manuscript. All authors contributed to the discussion and preparation of this manuscript.

Conflicts of interest

There are no conflicts to declare.

Acknowledgements

This work was supported by Natural Science Foundation of China (Grant No. 51821001, 11704245) and Natural Science Foundation of Shanghai (19ZR1475200). P. L. is supported by the Program for Professor of Special Appointment (Eastern Scholar) at Shanghai Institutions of Higher Learning. M. C. is sponsored by the Whiting School of Engineering, Johns Hopkins University and National Science Foundation (NSF DMR-1804320). We thank Yuxiao Zhu for generous help with LED arrays, Zhenying Chen and Junjie Ding for help with analysis and discussion of EXAFS data.

References

- [1] Q. Zhang and J. Guan, *Adv. Func. Mater.*, 2020, **30**, 2000768.
- [2] M. Liu, L. Wang, K. Zhao, S. Shi, Q. Shao, L. Zhang, X. Sun, Y. Zhao and J. Zhang, *Energy Environ. Sci.*, 2019, **12**, 2890-2923.
- [3] C.W.B. Bezerra, L. Zhang, K. Lee, H. Liu, A.L.B. Marques, E.P. Marques, H. Wang and J. Zhang, *Electrochim. Acta*, 2008, **53**, 4937-4951.
- [4] D. Astruc, F. Lu and J.R. Aranzaes, *Angew. Chem. Int. Ed.*, 2005, **44**, 7852-7872.
- [5] Q.-Q. Yan, D.-X. Wu, S.-Q. Chu, Z.-Q. Chen, Y. Lin, M.-X. Chen, J. Zhang, X.-J. Wu and

- H.-W. Liang, *Nat. Commun.*, 2019, **10**, 4977.
- [6] J.G. Lee, J. Hwang, H.J. Hwang, O.S. Jeon, J. Jang, O. Kwon, Y. Lee, B. Han and Y.-G. Shul, *J. Am. Chem. Soc.*, 2016, **138**, 3541-3547.
- [7] S. Back, A.R. Kulkarni and S. Siahrostami, *ChemCatChem*, 2018, **10**, 3034-3039.
- [8] J. Sun, S.E. Lowe, L. Zhang, Y. Wang, K. Pang, Y. Wang, Y. Zhong, P. Liu, K. Zhao, Z. Tang and H. Zhao, *Angew. Chem. Int. Ed.*, 2018, **57**, 16511-16515.
- [9] F.-L. Meng, K.-H. Liu, Y. Zhang, M.-M. Shi, X.-B. Zhang, J.-M. Yan and Q. Jiang, *Small*, 2018, **14**, 1703843.
- [10] C.-C. Hou, H.-F. Wang, C. Li and Q. Xu, *Energy Environ. Sci.*, 2020, **13**, 1658-1693.
- [11] H. Jiang, J. Gu, X. Zheng, M. Liu, X. Qiu, L. Wang, W. Li, Z. Chen, X. Ji and J. Li, *Energy Environ. Sci.*, 2019, **12**, 322-333.
- [12] H.-X. Zhong, Y. Zhang and X.-B. Zhang, *Chem*, 2018, **4**, 196-198.
- [13] H.-X. Zhong, K. Li, Q. Zhang, J. Wang, F.-L. Meng, Z.-J. Wu, J.-M. Yan and X.-B. Zhang, *NPG Asia Materials*, 2016, **8**, e308.
- [14] D. Zhang, W. Chen, Z. Li, Y. Chen, L. Zheng, Y. Gong, Q. Li, R. Shen, Y. Han, W.-C. Cheong, L. Gu and Y. Li, *ChemComm*, 2018, **54**, 4274.
- [15] X. Lv, Y. Chen, Y. Wu, H. Wang, X. Wang, C. Wei, Z. Xiao, G. Yang and J. Jiang, *J. Mater. Chem. A*, 2019, **7**, 27089-27098.
- [16] Z.-L. Wang, D. Xu, H.-X. Zhong, J. Wang, F.-L. Meng and X.-B. Zhang, *Science Advances*, 2015, **1**, e1400035.
- [17] H.-X. Zhong, J. Wang, Y.-W. Zhang, W.-L. Xu, W. Xing, D. Xu, Y.-F. Zhang and X.-B. Zhang, *Angew. Chem. Int. Ed.*, 2014, **53**, 14235-14239.
- [18] G. Wu, A. Santandreu, W. Kellogg, S. Gupta, O. Ogoke, H. Zhang, H.-L. Wang and L. Dai, *Nano Energy*, 2016, **29**, 83-110.
- [19] L. Zhong and S. Li, *ACS Catal.*, 2020, **10**, 4313-4318.
- [20] M. Lefèvre, E. Proietti, F. Jaouen and J.-P. Dodelet, *Science*, 2009, **324**, 71.
- [21] J. Han, J. Bian and C. Sun, *Research*, 2020, **2020**, 9512763.
- [22] G. Wu, K.L. More, C.M. Johnston and P. Zelenay, *Science*, 2011, **332**, 443.
- [23] J. Zhang, G. Chen, K. Müllen and X. Feng, *Adv. Mater.*, 2018, **30**, 1800528.
- [24] H. Fei, J. Dong, Y. Feng, C.S. Allen, C. Wan, B. Voloskiy, M. Li, Z. Zhao, Y. Wang, H. Sun, P. An, W. Chen, Z. Guo, C. Lee, D. Chen, I. Shakir, M. Liu, T. Hu, Y. Li, A.I. Kirkland, X. Duan and Y. Huang, *Nat. Catal.*, 2018, **1**, 63-72.
- [25] F. Meng, H. Zhong, D. Bao, J. Yan and X. Zhang, *J. Am. Chem. Soc.*, 2016, **138**, 10226-10231.

- [26] Y. Wang, X. Zhang, S. Xi, X. Xiang, Y. Du, P. Chen, D. Lyu, S. Wang, Z.Q. Tian and P.K. Shen, *ACS Sustain. Chem. Eng.*, 2020, **8**, 9367-9376.
- [27] J. Liu, M. Jiao, L. Lu, H.M. Barkholtz, Y. Li, Y. Wang, L. Jiang, Z. Wu, D.-j. Liu, L. Zhuang, C. Ma, J. Zeng, B. Zhang, D. Su, P. Song, W. Xing, W. Xu, Y. Wang, Z. Jiang and G. Sun, *Nat. Commun.*, 2017, **8**, 15938.
- [28] J. Han, G. Huang, Z. Wang, Z. Lu, J. Du, H. Kashani and M. Chen, *Adv. Mater.*, 2018, **30**, 1803588.
- [29] M. Shen, C. Wei, K. Ai and L. Lu, *Nano Res*, 2017, **10**, 1449-1470.
- [30] J. Wang, Z. Huang, W. Liu, C. Chang, H. Tang, Z. Li, W. Chen, C. Jia, T. Yao, S. Wei, Y. Wu and Y. Li, *J. Am. Chem. Soc.*, 2017, **139**, 17281-17284.
- [31] D. Liu, B. Wang, H. Li, S. Huang, M. Liu, J. Wang, Q. Wang, J. Zhang and Y. Zhao, *Nano Energy*, 2019, **58**, 277-283.
- [32] X. Wan, R. Wu, J. Deng, Y. Nie, S. Chen, W. Ding, X. Huang and Z. Wei, *J. Mater. Chem. A*, 2018, **6**, 3386-3390.
- [33] Z. Zhu, H. Yin, Y. Wang, C.-H. Chuang, L. Xing, M. Dong, Y.-R. Lu, G. Casillas-Garcia, Y. Zheng, S. Chen, Y. Dou, P. Liu, Q. Cheng and H. Zhao, *Adv. Mater.*, 2020, **n/a**, 2004670.
- [34] X. Guo, J. Gu, S. Lin, S. Zhang, Z. Chen and S. Huang, *J. Am. Chem. Soc.*, 2020, **142**, 5709-5721.
- [35] Y. Ying, X. Luo, J. Qiao and H. Huang, *Adv. Funct. Mater.*, **n/a**, 2007423.
- [36] H.J. Qiu, Y. Ito, W. Cong, Y. Tan, P. Liu, A. Hirata, T. Fujita, Z. Tang and M. Chen, *Angew. Chem. Int. Ed.*, 2015, **54**, 14031-14035.
- [37] H.-J. Qiu, P. Du, K. Hu, J. Gao, H. Li, P. Liu, T. Ina, K. Ohara, Y. Ito and M. Chen, *Adv. Mater.*, 2019, **31**, 1900843.
- [38] Y. Ito, Y. Tanabe, H.-J. Qiu, K. Sugawara, S. Heguri, N.H. Tu, K.K. Huynh, T. Fujita, T. Takahashi, K. Tanigaki and M. Chen, *Angew. Chem. Int. Ed.*, 2014, **53**, 4822-4826.
- [39] Z. Yang, B. Chen, W. Chen, Y. Qu, F. Zhou, C. Zhao, Q. Xu, Q. Zhang, X. Duan and Y. Wu, *Nat. Commun.*, 2019, **10**, 3734.
- [40] P. Liu, P. Guan, A. Hirata, L. Zhang, L. Chen, Y. Wen, Y. Ding, T. Fujita, J. Erlebacher and M. Chen, *Adv. Mater.*, 2016, **28**, 1753-1759.
- [41] L. Chen, J. Han, Y. Ito, T. Fujita, G. Huang, K. Hu, A. Hirata, K. Watanabe and M. Chen, *Angew. Chem. Int. Ed.*, 2018, **57**, 13302-13307.
- [42] Y. Ito, Y. Shen, D. Hojo, Y. Itagaki, T. Fujita, L. Chen, T. Aida, Z. Tang, T. Adschiri and M. Chen, *Adv. Mater.*, 2016, **28**, 10644-10651.
- [43] Rubén Rozada, Juan I. Paredes, Silvia Villar-Rodil, Amelia Martínez-Alonso and Juan M.

D. Tascón, *Nano Res.* 2013, **6**, 216.

[44] G. Chen, P. Liu, Z. Liao, F. Sun, Y. He, H. Zhong, T. Zhang, E. Zschech, M. Chen, G. Wu, J. Zhang and X. Feng, *Adv. Mater.*, 2020, **32**, 1907399.

[45] Q. Han, H. Shan, J. Deng, A. Zhao, B. Wang and J. G. Hou, *Nanoscale*, 2014, **6**, 7934-7939.

[46] J. Charlier, V. Detalle, F. Valin, C. Bureau, and G. Le'cayon, *J. Vac. Sci. Technol.*, 1997, **15**, 353.

[47] L. Gao, M. Zhang, H. Zhang and Z. Zhang, *J. Power Sources*, 2020, **450**, 227577.

[48] J. Wang, W. Liu, G. Luo, Z. Li, C. Zhao, H. Zhang, M. Zhu, Q. Xu, X. Wang, C. Zhao, Y. Qu, Z. Yang, T. Yao, Y. Li, Y. Lin, Y. Wu and Y. Li, *Energy Environ. Sci.* 2018, **11**, 3375-3379.

[49] J. Chen, H. Li, C. Fan, Q. Meng, Y. Tang, X. Qiu, G. Fu and T. Ma, *Adv. Mater.*, 2020, **33**, 2003134.

[50] H. Shang, X. Zhou, J. Dong, A. Li, X. Zhao, Q. Liu, Y. Lin, J. Pei, Z. Li, Z. Jiang, D. Zhou, L. Zheng, Y. Wang, J. Zhou, Z. Yang, R. Cao, R. Sarangi, T. Sun, X. Yang, X. Zheng, W. Yan, Z. Zhuang, J. Li, W. Chen, D. Wang, J. Zhang and Y. Li, *Nat. Commun.*, 2020, **11**, 3049.

[51] S. Ma, Z. Han, K. Leng, X. Liu, Y. Wang, Y. Qu and J. Bai, *Small*, 2020, **16**, 2001384.

[52] Y. Qu, Z. Li, W. Chen, Y. Lin, T. Yuan, Z. Yang, C. Zhao, J. Wang, C. Zhao, X. Wang, F. Zhou, Z. Zhuang, Y. Wu and Y. Li, *Nat. Catal.*, 2018, **1**, 781-786.

[53] H. Wu, H. Li, X. Zhao, Q. Liu, J. Wang, J. Xiao, S. Xie, R. Si, F. Yang, S. Miao, X. Guo, G. Wang and X. Bao, *Energy Environ. Sci.*, 2016, **9**, 3736-3745.

[54] D. Karapinar, N.T. Huan, N. Ranjbar Sahraie, J. Li, D. Wakerley, N. Touati, S. Zanna, D. Taverna, L.H. Galvão Tizei, A. Zitolo, F. Jaouen, V. Mougél and M. Fontecave, *Angew. Chem. Int. Ed.*, 2019, **58**, 15098-15103.

[55] K. Jiang, S. Siahrostami, T. Zheng, Y. Hu, S. Hwang, E. Stavitski, Y. Peng, J. Dynes, M. Gangisetty, D. Su, K. Attenkofer and H. Wang, *Energy Environ. Sci.*, 2018, **11**, 893-903.

[56] L. Jiao, G. Wan, R. Zhang, H. Zhou, S.-H. Yu and H.-L. Jiang, *Angew. Chem. Int. Ed.*, 2018, **57**, 8525-8529.

[57] Z. Yang, Y. Wang, M. Zhu, Z. Li, W. Chen, W. Wei, T. Yuan, Y. Qu, Q. Xu, C. Zhao, X. Wang, P. Li, Y. Li, Y. Wu and Y. Li, *ACS Catal.*, 2019, **9**, 2158-2163.

[58] L. Yang, H. Xu, H. Liu, X. Zeng, D. Cheng, Y. Huang, L. Zheng, R. Cao and D. Cao, *Research*, 2020, **2020**, 12

Figures and Captions

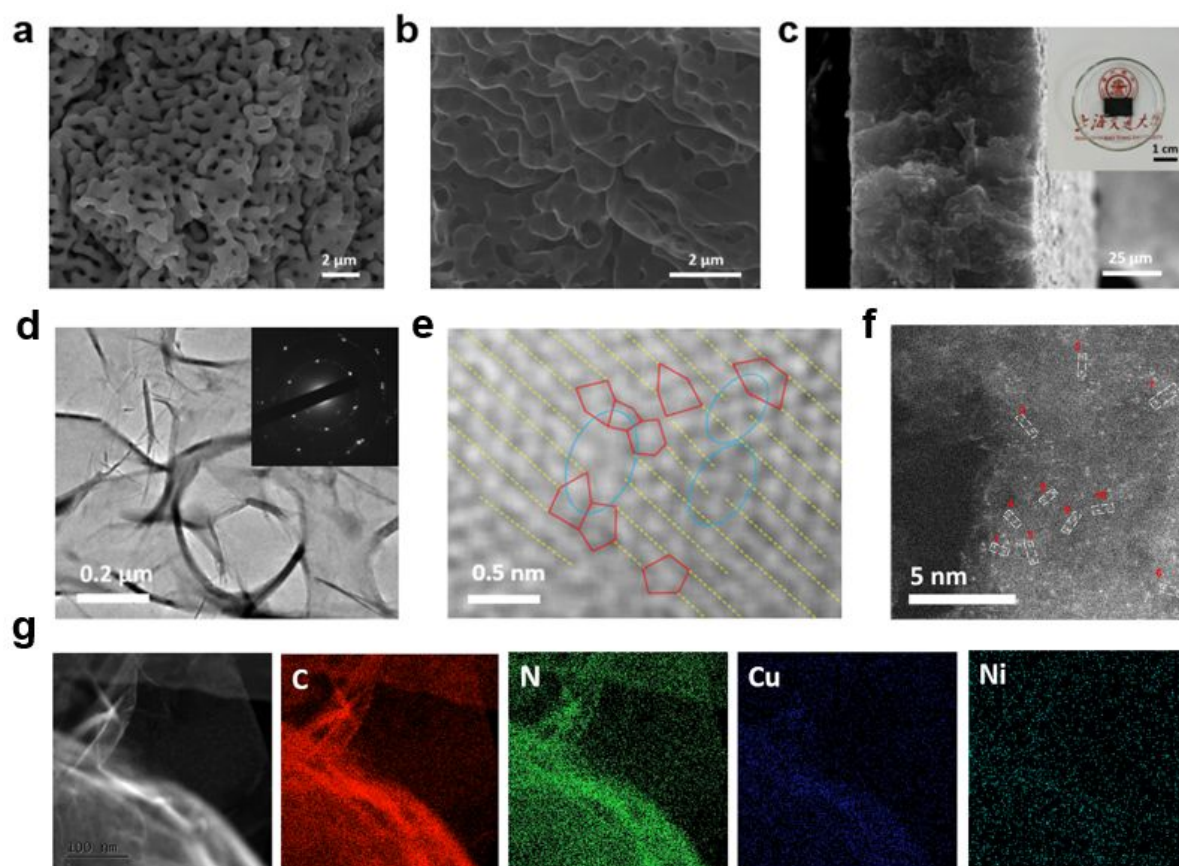


Fig. 1 (a,b) SEM images of nanoporous nickel coated with nitrogen doped graphene (np-Ni@NG) and Ni single atoms anchored nitrogen doped graphene (Ni-NG) after hydrochloric acid etching. (c) Cross-sectional view of the free-standing Ni-NG. The inset shows an optical image of Ni-NG with the size of 2 cm × 1.4 cm. (d) TEM image of (Ni,Cu)-NG. Inset: selected area electron diffraction pattern. (e) Defective carbon hexagon structure of (Ni,Cu)-NG. (f) Cs-corrected HAADF-STEM image of (Ni,Cu)-NG. The bright dots correspond to Ni and Cu single atoms. Several single atoms and their neighboring single atoms are highlighted by white rectangles. (g) HAADF-STEM image and corresponding EDS mappings of C, N, Cu and Ni.

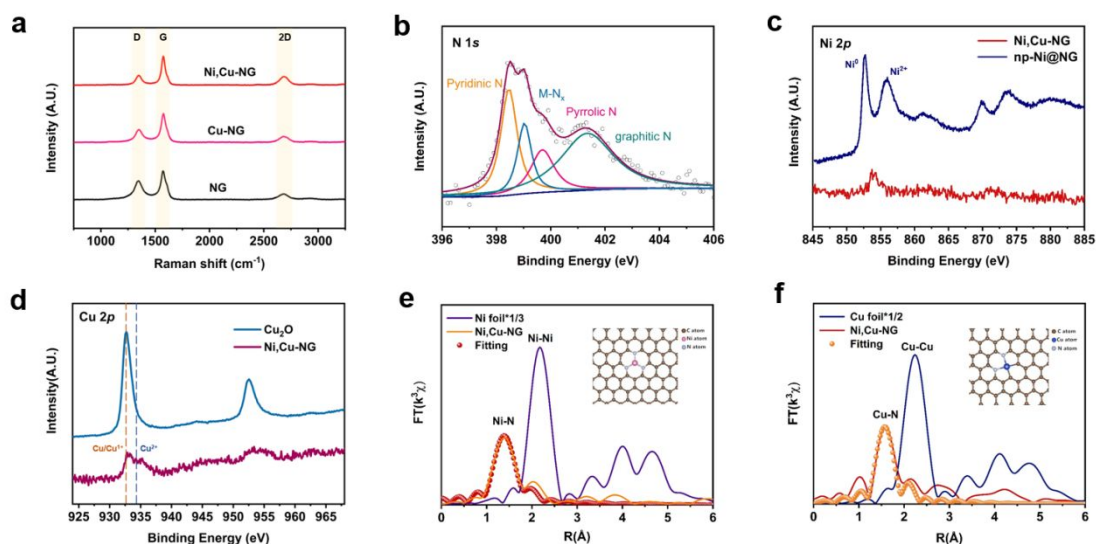


Fig. 2 (a) Raman spectra of (Ni,Cu)-NG, Cu-NG and NG. (b) High resolution N 1s XPS spectrum of (Ni,Cu)-NG. (c) Ni 2p XPS spectrum of (Ni,Cu)-NG and np-Ni@NG. (d) High resolution Cu 2p XPS spectra of (Ni,Cu)-NG and cuprous oxide (Cu_2O). The intensity of Cu_2O was divided by 2 for a better illustration. (e) Fourier-transformed k^3 -weighted EXAFS spectrum of the Ni-K edge for Ni foil (purple), (Ni,Cu)-NG (orange) and corresponding fitting curve. The inset shows the Ni-N₃ configuration used for EXAFS fitting. (f) Fourier-transformed k^3 -weighted EXAFS spectra of the Cu-K edge for Cu foil (blue), (Ni,Cu)-NG (red) and corresponding fitting curve. The inset shows the Cu-N₂-C₂ model used for EXAFS fitting.

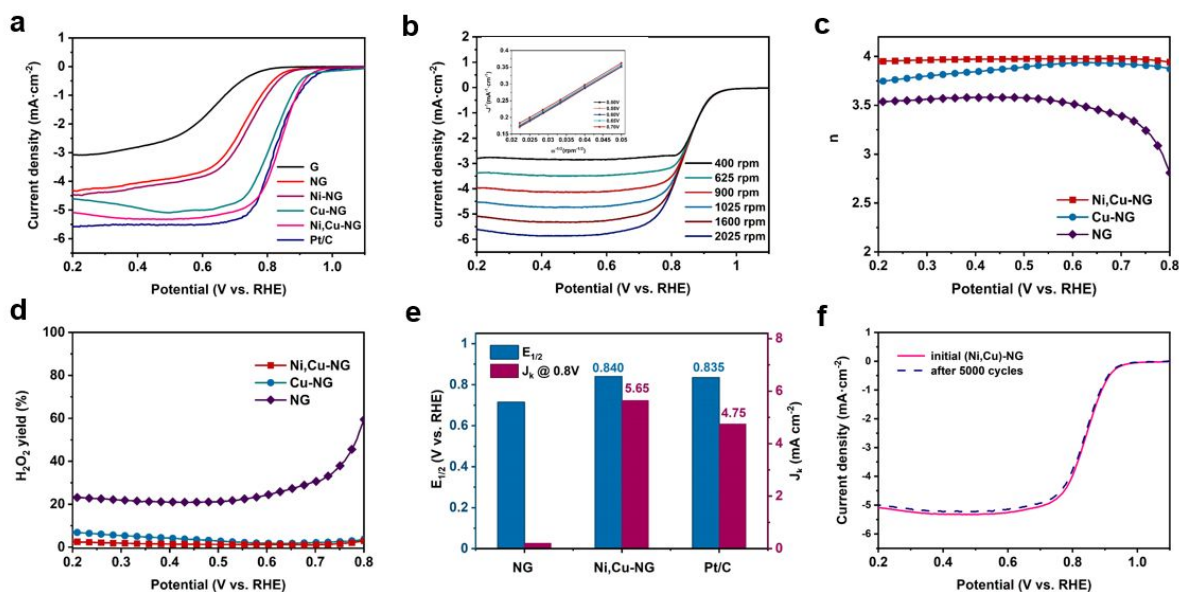


Fig. 3 (a) ORR polarization curves of G, NG, Ni-NG, Cu-NG, (Ni,Cu)-NG and Pt/C in 0.1M O₂-saturated KOH at the rotating speed of 1600 rpm with the sweep rate of 100 mV s⁻¹. (b) Polarization curves of (Ni,Cu)-NG at different rotating speeds ranging from 400 rpm to 2025 rpm. The inset shows corresponding Koutecky-Levich plots at various potentials. (c,d) Electron transfer number (n) and H₂O₂ yield of NG, Cu-NG and (Ni,Cu)-NG derived from RRDE. (e) Half-wave potential $E_{1/2}$ and kinetic current density J_k at 0.80 V of different catalysts. (f) Oxygen reduction reaction polarization curves of (Ni,Cu)-NG before (solid line) and after 5000 CV cycles (dash line) in the electrochemical accelerated durability test.

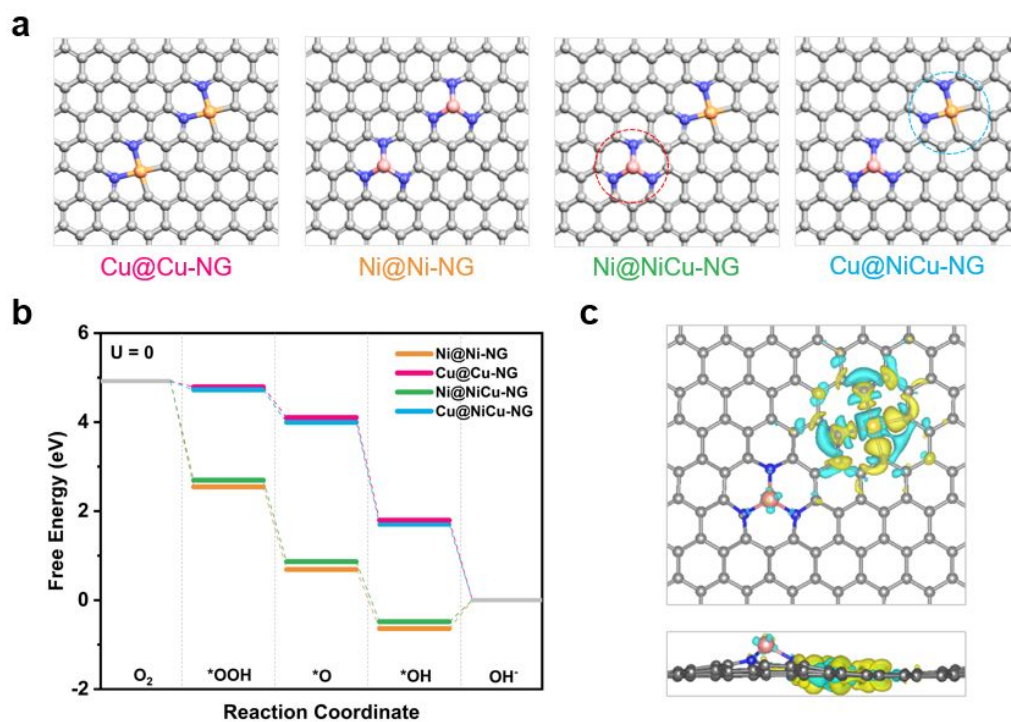


Fig. 4 Theoretical investigation of ORR activity on different active sites. (a) Different active sites for theoretical simulations. Gray: C; blue: N; light red: Ni; orange: Cu. (b) Free energy profile of ORR on different active sites. (c) Top and side views of differential charge density of Cu@NiCu-NG active sites.

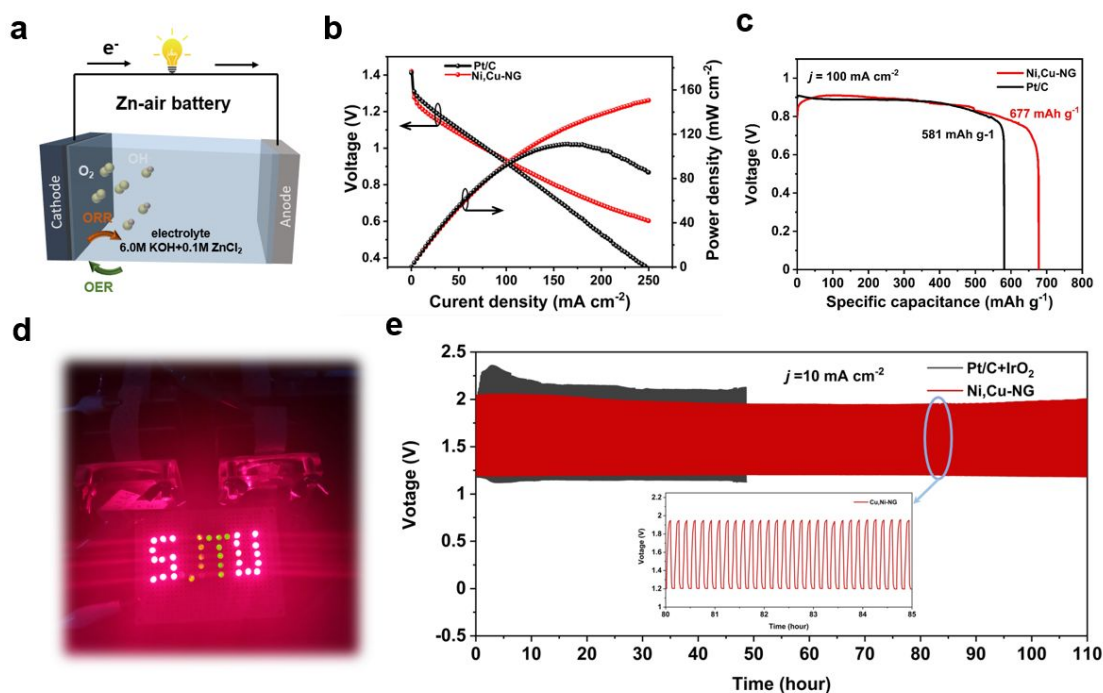


Fig. 5 (a) Schematic diagram of the rechargeable Zn-air battery. (b) Discharge polarization curves of (Ni,Cu)-NG based and Pt/C based Zn-air batteries and the corresponding power density curves. (c) Long-time galvanostatic discharge curves of (Ni,Cu)-NG based and Pt/C based Zn-air batteries at the discharge current density of 100 mA cm^{-2} . The specific capacities were normalized to the mass of consumed zinc plate. (d) Photograph of LED arrays powered by two (Ni,Cu)-NG based Zn-air batteries connected in series. (e) Charge and discharge cycling curves of Zn-air battery at 10 mA cm^{-2} .